Contact area and size effects in discrete dislocation modeling of wedge indentation

Widjaja, Andreas; van der Giessen, Erik; Deshpande, Vikram S.; Needleman, Alan

Published in:
Journal of Materials Research

DOI:
10.1557/JMR.2007.0090

Publication date:
2007

Contact area and size effects in discrete dislocation modeling of wedge indentation

Andreas Widjaja and Erik Van der Giessen[a)]
University of Groningen, Department of Applied Physics, Nijenborgh 4, 9747 AG, Groningen, The Netherlands

Vikram S. Deshpande
University of Cambridge, Engineering Department, Cambridge CB2 1PZ, United Kingdom

Alan Needleman
Brown University, Division of Engineering, Providence, Rhode Island 02912

(Received 28 July 2006; accepted 31 October 2006)

Plane strain indentation of a single crystal by a rigid wedge is analyzed using discrete dislocation plasticity. We consider two wedge geometries having different sharpness, as specified by the half-angle of the indenter: $\alpha = 70°$ and 85°. The dislocations are all of edge character and modeled as line singularities in a linear elastic material. The crystal has initial sources and obstacles randomly distributed over three slip systems. The lattice resistance to dislocation motion, dislocation nucleation, dislocation interaction with obstacles, and dislocation annihilation are incorporated through a set of constitutive rules. Several definitions of the contact area (contact length in plane strain) are used to illustrate the sensitivity of the hardness value in the submicron indentation regime to the definition of contact area. The size dependence of the indentation hardness is found to be sensitive to the definition of contact area used and to depend on the wedge half-angle. For a relatively sharp indenter, with a half-angle of 70°, an indentation size effect is not obtained when the contact area is small and when the hardness is based on the actual contact length, while there does appear to be a size effect for some hardness values based on other measures of contact length.

I. INTRODUCTION

Indentation is commonly used for measuring material properties such as Young's modulus and hardness. At a sufficiently small scale, the indentation hardness can be size dependent,[1–4] which is not predicted by classical continuum plasticity. Various frameworks have been used to model indentation size effects, such as molecular dynamics,[5] strain gradient plasticity,[6–9] and dislocation dynamics.[10–14] Discrete dislocation plasticity is well-suited for modeling the deformation of crystalline solids in the submicrometer scale regime. It thus provides a framework for analyzing phenomena between the nanoindentation and the size-independent continuum regimes.

The key parameter to extract from indentation tests in plastically deforming solids is the hardness or the mean indentation pressure, i.e., the ratio between indentation force and contact area. While the contact area is difficult to measure experimentally, Oliver and Pharr[15] devised a method for sharp indenters, which makes use of the unloading stiffness to infer the actual contact area. This approach has become the standard in nano- and microscale indentation.[4,16] It is based on the geometric self-similarity of sharp indenters, a well-known square-root scaling law for the contact stiffness of three-dimensional (3D) indenters and the assumption that sink-in is purely elastic. Even though such a scaling law does not exist for two-dimensional (2D) wedge indentation, recent discrete dislocation studies[14] have indicated that the Oliver–Pharr procedure can be used to estimate the contact area (in two dimensions, the contact length times a unit thickness), even when unloading is not purely elastic. It was also found in this study that the contact length determined from the computation was smaller than the one estimated using the Oliver–Pharr procedure.

Because plastic slip is a discrete event, dislocation plasticity under the indenter can give rise to the development of a rough surface having patches under the indenter where there is no traction transmitted between the indenter and the material. When contact is defined as the region where traction is being transmitted, these

[a)]Address all correspondence to this author.
e-mail: e.van.der.giessen@rug.nl
DOI: 10.1557/JMR.2007.0090

traction-free patches reduce the actual contact area. Hence, there are a variety of possible quantities that can be used as a measure of contact area: (i) the nominal contact area obtained by projection, (ii) the measure of contact area according to the Oliver–Pharr procedure, (iii) the smooth-surface contact area, and (iv) the contact area accounting for surface roughness. In this study, we carried out plane strain discrete dislocation analyses of wedge indentation. The results show that the various definitions of contact area (or equivalently in plane strain, contact length) lead to different hardness values and, in addition, lead to significant variations in the predicted indentation size effect.

II. DISCRETE DISLOCATION FORMULATION

Here, we analyze the plane strain wedge indentation of a single crystal. The crystal is taken to be elastically isotropic with Young's modulus E and Poisson's ratio ν. It has three slip systems at angles $\phi^{(\beta)} = \{35.3°, 90.0°, 144.7°\}$ relative to the free top surface, which corresponds to a face-centered cubic (fcc) crystal with the (110)-plane parallel to the x_1–x_2 plane of consideration. Plasticity is a result of the collective motion of edge dislocations with magnitude b of the Burgers vector. The displacement discontinuity in between each dislocation dipole (the 2D equivalent of a dislocation loop) contributes to what is observed as plastic strain on a larger length scale; plastic strain increases as the number of dipoles per unit area and their size increase. The dislocations are treated as line singularities in a linear elastic continuum with their motion and evolution being governed by a set of constitutive rules.[17]

Superposition is used to calculate the stress and deformation state at each stage.[18] This method combines the ($\tilde{}$) field caused by dislocations, calculated analytically from the linear isotropic elastic dislocation fields, and a smooth image field ($\hat{}$) that corrects the solutions to satisfy the boundary conditions. The displacements u_i, strains ϵ_{ij}, and stresses σ_{ij} are written as

$$u_i = \hat{u}_i + \tilde{u}_i \quad ,$$
$$\epsilon_{ij} = \hat{\epsilon}_{ij} + \tilde{\epsilon}_{ij} \quad ,$$
$$\sigma_{ij} = \hat{\sigma}_{ij} + \tilde{\sigma}_{ij} \quad , \tag{1a}$$

where the ($\tilde{}$) field is the sum of the fields of the individual dislocations in their current positions, i.e.,

$$\tilde{u}_i = \sum_{J=1}^{N} \tilde{u}_i^{(J)} \quad ,$$
$$\tilde{\epsilon}_{ij} = \sum_{J=1}^{N} \tilde{\epsilon}_{ij}^{(J)} \quad ,$$
$$\tilde{\sigma}_{ij} = \sum_{J=1}^{N} \tilde{\sigma}_{ij}^{(J)} \quad . \tag{1b}$$

We use the finite element method to solve a linear elastic boundary value problem to obtain the image fields.

The indentation computations start with a dislocation-free crystal having sources and obstacles that are randomly placed on the slip planes. When the resolved shear stress at a source location is large enough, $\tau \geq \tau_{\text{nuc}}$, for a sufficiently long time, $t \geq t_{\text{nuc}}$, a dislocation dipole with Burgers vector $\pm b$ is nucleated separated by a distance L_{nuc}. This mimics the Frank–Read mechanism in two dimensions.

If two dislocations of opposite sign come within a critical distance L_e on a slip plane, they annihilate.

Glide of a dislocation I is controlled by the Peach–Koehler force, whose component in the slip direction is calculated as

$$f^{(I)} = m_i^{(I)} \left(\hat{\sigma}_{ij} + \sum_{J \neq I} \tilde{\sigma}_{ij}^{(J)} \right) b_j^{(I)} \quad , \tag{2}$$

where $m_i^{(I)}$ is the unit normal vector to the slip system containing the dislocation with Burgers vector $b_j^{(I)}$. Assuming drag-controlled glide, the glide velocity is given by

$$v^{(I)} = f^{(I)}/B \quad , \tag{3}$$

where B is the drag coefficient.

When a dislocation meets an obstacle, it is pinned there and released only when the Peach–Koehler force exceeds $b\tau_{\text{obs}}$.

III. GEOMETRY

A planar crystal of dimensions $2L_1 = 200$ μm by $L_2 = 200$ μm is considered symmetric with respect to the plane $x_1 = 0$ and is indented by a rigid wedge along the x_2 axis (see Fig. 1). The crystal is taken to be fully clamped at $x_2 = L_2$, while the side $x_1 = L_1$ is kept traction free.

Plastic deformation takes place inside a process window $l_1 \times l_2 = 25$ μm × 50 μm (Fig. 1) to limit the computational burden. The size of this window does not affect the results other than limiting the size of the plastic zone: the calculation ends when or before a dislocation reaches the edge of the process window. The Burgers vector magnitude is taken to have the value $b = 0.25$ nm, typical for aluminum, and the active slip planes are spaced $100b$ apart. With the slip planes at $\phi^{(\beta)} = \{35.3°, 90.0°, 144.7°\}$, the crystal is subject to symmetric slip (Fig. 2), and only the region $x_1 \geq 0$ is analyzed.

The finite element mesh is highly refined near the indenter tip, to accurately represent the contact region, as shown in the inset of Fig. 1. For the indenter with wedge angle $\alpha = 85°$, the element size on the surface is 0.5 nm while for $\alpha = 70°$, where the contact length tends to be smaller, the element length is as small as 0.24 nm, i.e., comparable to the size of the Burgers vector.

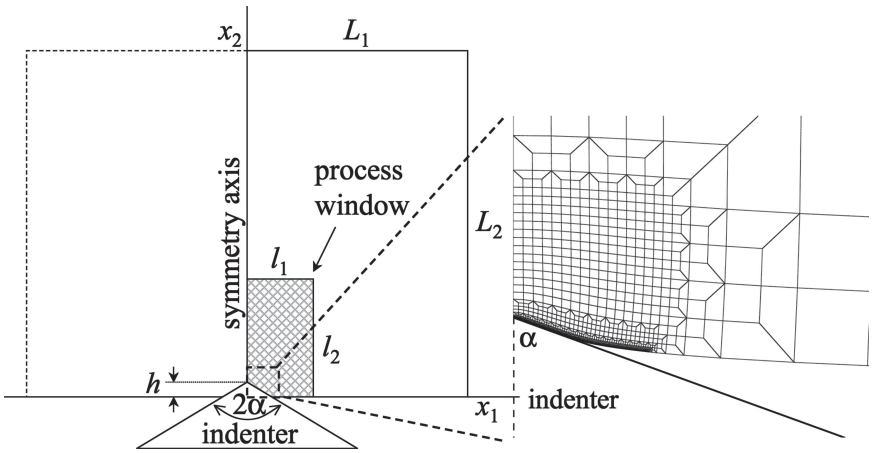

FIG. 1. Schematic diagram of the model. Planar symmetric single crystal indented with wedge indenter at a depth h. The tip angle of the wedge indenter is 2α. The total area of the crystal is 16 times larger than the process window. The finite element mesh (see the zoomed area) is highly refined near the tip.

IV. DETERMINATION OF CONTACT AREA

In plane strain, the contact area at a certain indentation depth h is determined by the contact length in the plane of deformation. The simplest measure of contact length is the nominal contact length a_N, which is the projection of the indenter on the x_1-axis, i.e.,

$$a_N = h \tan \alpha \quad .$$

The actual contact length α_A is defined as

$$a_A = \int_{x \in S_c} dx \quad , \tag{4}$$

where S_c is the surface in contact, defined as the portions of the surface which are in contact with the indenter and which transmit traction that contributes to the indentation force (S_c evolves during indentation and is determined through a contact algorithm that will be described subsequently). We approximate a_A by summing all the finite-element segments in contact, i.e.,

$$a_A \approx \sum_i \Delta s_1^{(i)} \quad , \tag{5}$$

where $\Delta s_1^{(i)}$ is the projected length on the x_1-axis of ith segment, which is in contact with the indenter. As long as the surface in contact is smooth, a_A is identical to the end-to-end contact length, which is the distance between the farthest node in contact with the indenter and x_2-axis. When the surface is rough, the end-to-end contact length a_E exceeds the actual contact length a_A. The difference between the two is illustrated in Fig. 3. The ratio a_E/a_A serves as a simple measure of roughness, with values of this ratio being larger than unity for a rough contact surface.

We also consider the estimate of contact length, proposed by Oliver and Pharr,[15] that is widely used in experiments. The Oliver–Pharr method uses an unloading procedure with the assumption that the initial unloading response is elastic and the sink-in of the material can be modeled as elastic indentation of a substrate by a rigid

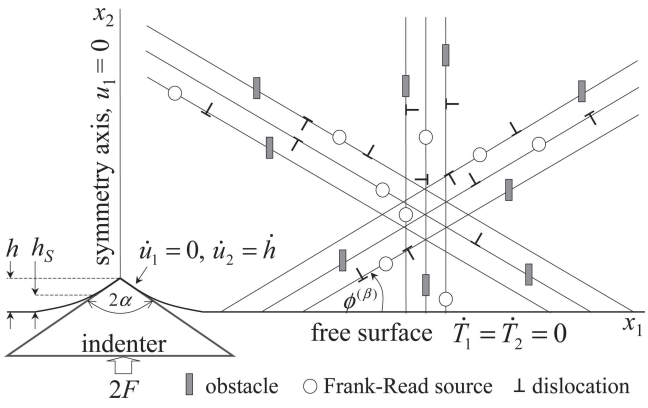

FIG. 2. Schematic diagram with boundary conditions of the microscopic model in the process window (Fig. 1) at indentation depth h. The sink-in depth is h_S. Dislocations, Frank–Read sources, and dislocation obstacles are living on slip planes in the process window.

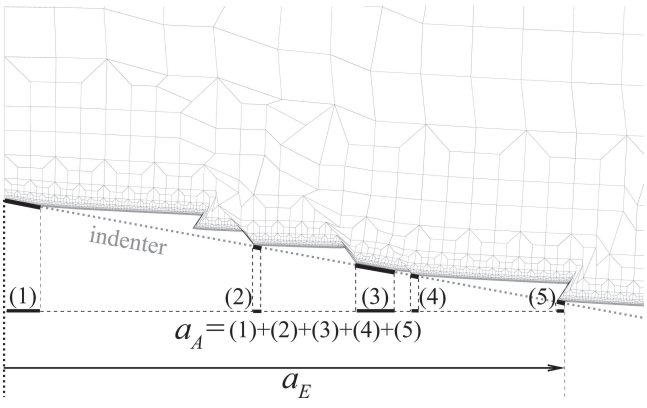

FIG. 3. Illustration of the determination of the actual contact length a_A for an indenter in contact with a rough surface. For comparison, the end-to-end contact length a_E is also indicated. The dimensions are not necessarily to scale for illustrative purposes.

indenter having a simple geometry. The procedure involves calculating the unloading stiffness

$$S := \mathrm{d}F/\mathrm{d}h|_{F=F\max} \quad ,$$

at initial unloading and then determining the sink-in depth h_S as

$$h_S = \eta \frac{E_{\max}}{S} \quad , \tag{6}$$

where η depends on the geometry of the indenter. Finally, by geometry, the contact length a_S at the indentation force $F_{\max}$ is estimated as

$$a_S = (h - h_S)\tan\alpha \quad . \tag{7}$$

In three dimensions, the Oliver–Pharr method is based on the scaling relation $S \propto E\sqrt{A}$ for self-similar indentation, where A is the contact area. In two dimensions such a direct, simple relationship between S and the contact area does not exist. Instead, for a finite-sized block, the elastic compliance depends on its dimensions and the boundary conditions so that $S \propto gE$, where g is a nondimensional function of contact area (or indentation depth) and block size. However, in both three and two dimensions, the contact stiffness S is assumed to be proportional with Young's modulus E. Moreover, Eq. (6) is based on the assumption that sink-in is elastic; the issue here is if and how possible plastic deformation during unloading affects this relation.

For application of the Oliver–Pharr approach in our discrete dislocation simulations, we first calculate the unloading stiffness S as a function of depth h from an elastic loading–unloading indentation curve. Because elastic indentation is reversible, unloading and loading curves are identical for a given indenter. We choose the following expression to fit the elastic indentation force F as a function of indentation depth h:

$$F(h) = C_1 h + C_2 h^{3/2} + C_3 h^2 + C_4 h^{5/2} \quad . \tag{8}$$

The fitting parameters C_i for both wedge angles are given in Table I.

The correlation coefficients differ from the perfect-fit value 1.0 by only 10^{-7} and 3×10^{-7} for $\alpha = 70°$ and $\alpha = 85°$, respectively. The resulting stiffness function $S(h)$ is obtained by straightforward differentiation of Eq. (8). The quality of the fit [Eq. (8)] diminishes as $h \to 0$; to avoid inaccuracies caused by the fitting procedure, we will therefore not present results for contact lengths less than $h \approx 5$ nm. The variation of S with h is a consequence of the non-self-similarity of the solution for a finite-sized crystal, as considered here. Scaling arguments for a half space show that S for self-similar elastic indentation would be independent of h, but the half-space solution suffers from the fact that the displacement contains an irrecoverable logarithmic singularity.

TABLE I. (left) Values of the parameters C_1 through C_4 in the fit of $F(h)$ for elastic indentation according to Eq. (8) for indenters with two tip angles. (right) Values of the parameters D_1 through D_4 in the fit of $\eta(h)$ for elastic indentation according to Eq. (9) for both wedge angles.

F fit, Eq. (8)	$\alpha = 70°$	$\alpha = 85°$	η fit, Eq. (9)	
C_1 (μN μm^{-2})	4470	4940	D	1.163
C_2 (μN μm$^{-5/2}$)	7700	10430	D_2 (μm^{-1})	2169
C_3 (μN μm^{-3})	−6580	−8050	D_3 (μm^{-1})	2297
C_4 (μN μm$^{-7/2}$)	3300	4200	D_4 (μm^{-2})	109.0

For flat punches, the geometrical factor η in Eq. (6) is unity, but for wedges the ratio between computed sink-in h_S and $F_{\max}/S$ varies from 1.16 at small h to values between 0.95 and 0.92 for h up to 0.5 μm. There is no significant difference between the values for $\alpha = 70°$ and 85°. As discussed in the Appendix, the value of η is fit from the elastic indentation computation with a smooth function:

$$\eta(h) = \frac{D_1 + D_2 h}{1 + D_3 h + D_4 h^2} \quad , \tag{9}$$

with parameter values D_i specified in Table I. To determine the contact length during discrete dislocation plasticity computations, at any force $F_{\max}$, we calculate the value of the ratio S/η from Eqs. (8) and (9) at the corresponding depth h and calculate a_S from Eqs. (6) and (7). The variation of the unloading stiffness S/η with depth is included in Fig. 4.

V. BOUNDARY CONDITIONS

Although the computations assume small strains, we account for the evolving contact area through the following contact algorithm. At each increment in the

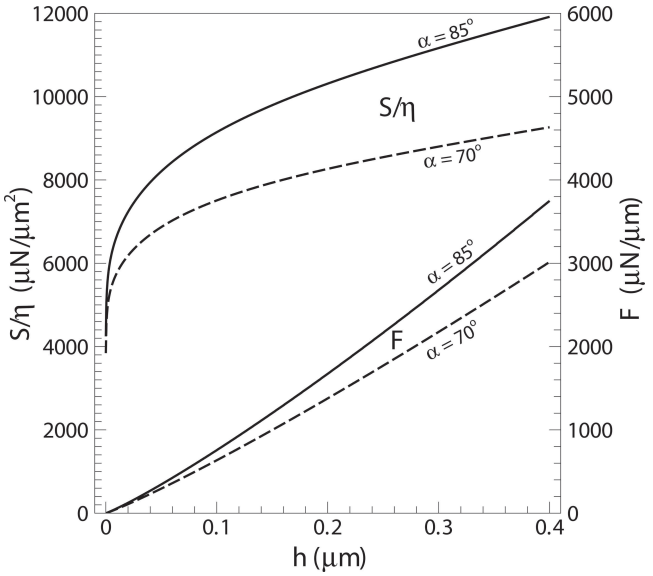

FIG. 4. Indentation force F and effective contact stiffness S/η versus depth h for elastic loading–unloading.

computation, the current contact region S_c is determined from the criterion that prevents interpenetration of the indenter and the crystal. The maximum $x_1 \in S_c$ determines the actual contact length a_A.

Indentation is imposed by prescribing the displacement rates on the contact surface S_c as

$$\dot{u}_1 = 0,\ \dot{u}_2 = \dot{h} \text{ on } S_c \quad , \tag{10}$$

assuming perfect sticking once the indenter comes in contact with the crystal. Here, a dot ($\dot{}$) denotes differentiation with respect to time. The other boundary conditions are

$$\dot{u}_1 = 0 \text{ on } x_1 = 0 \quad , \tag{11}$$

because of symmetry, and

$$\dot{T}_1 = \dot{T}_2 = 0 \text{ on } x_2 = 0 \notin S_c \quad . \tag{12}$$

Here, $T_i = \sigma_{ij} n_j$ is the traction on the surface with normal n_j directing outward from the surface. Note that in this way the boundary conditions near $x_2 = 0$ change from being governed by Eq. (12) to Eq. (10) as the material comes into contact with the indenter. The boundary value problem analyzed is sketched in Fig. 2.

The indentation force $2F$ (per unit length perpendicular to the plane of deformation) is obtained from the component T_2 of the surface traction $T_i = \sigma_{ij} n_j$ along the contact surface as

$$F = \int_{x \in S_c} T_2 \, \mathrm{d}x \quad . \tag{13}$$

VI. NUMERICAL RESULTS

All calculations are carried out using Young's modulus $E = 70$ GPa and Poisson's ratio $\nu = 0.33$, representative of aluminum. We use a source density $\rho_{nuc} = 49\ \mu m^{-2}$ and an obstacle density $\rho_{obs} = 99\ \mu m^{-2}$ as adopted in previous dislocation dynamics simulations.[14,17] The source strength τ_{nuc} follows a normal distribution with a mean value of 50 MPa and standard deviation of 10 MPa. The nucleation time of sources $t_{nuc} = 10$ ns. The obstacle strength τ_{obs} is set to be 150 MPa.

The indentation rate is taken to be high, $\dot{h} = 0.1\ ms^{-1}$, to limit computing times; the time step $\Delta t = 0.5$ ns is sufficiently small ($\Delta t \ll t_{nuc}$) that dislocation nucleation events are not missed out.

The predicted indentation force F versus depth h curves for the $\alpha = 70°$ and $\alpha = 85°$ indenters are shown in Fig. 5. The force for the $\alpha = 85°$ indenter is significantly greater than that for the $\alpha = 70°$ indenter once plastic flow occurs.

The evolution of the four measures of contact length is shown in Figs. 6 and 7 for the two wedge angles considered. To determine a_S, we use the geometrical relation in Eq. (7) with the sink-in depth h_S obtained from Eq. (6).

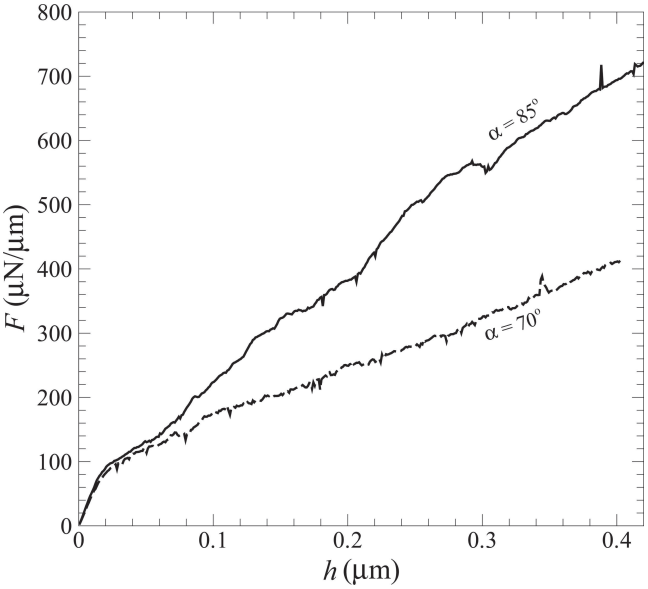

FIG. 5. Indentation force F versus depth h of discrete dislocation indentation calculation for two values of the half-angle of the wedge indenter.

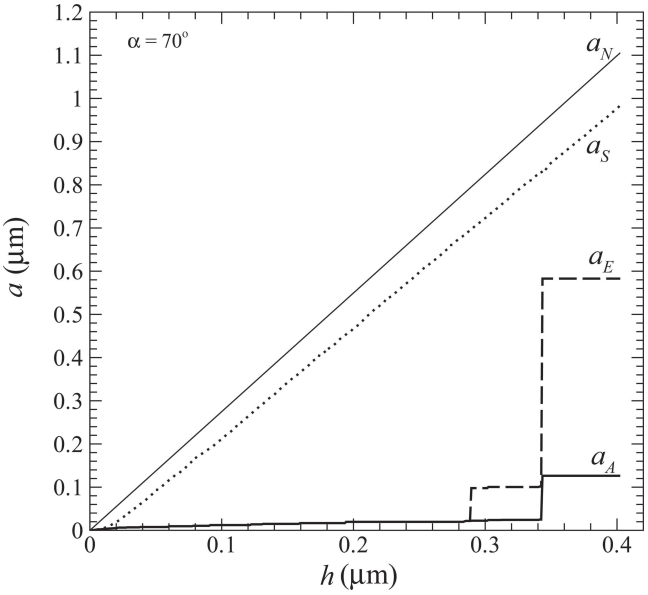

FIG. 6. Evolution of the four contact length measures (a_N, the nominal contact area; a_S, the Oliver–Pharr estimate; a_E, the end-to-end contact area; and a_A the actual contact area) versus depth h for wedge indenters with $\alpha = 70°$.

For both wedge angles, we use the value $\eta = h_S/(F_{max}/S)$ calculated for elastic indentation.

The difference between the nominal contact length a_N and the Oliver–Pharr estimate a_S is due only to sink-in, while the difference between a_S and the end-to-end contact length a_E is due to the fact that plastic slip caused by dislocation motion affects sink-in (and is neglected in the calculation of a_S) and that unloading is not purely elastic as assumed in Eqs. (6) and (7).[14] The difference between

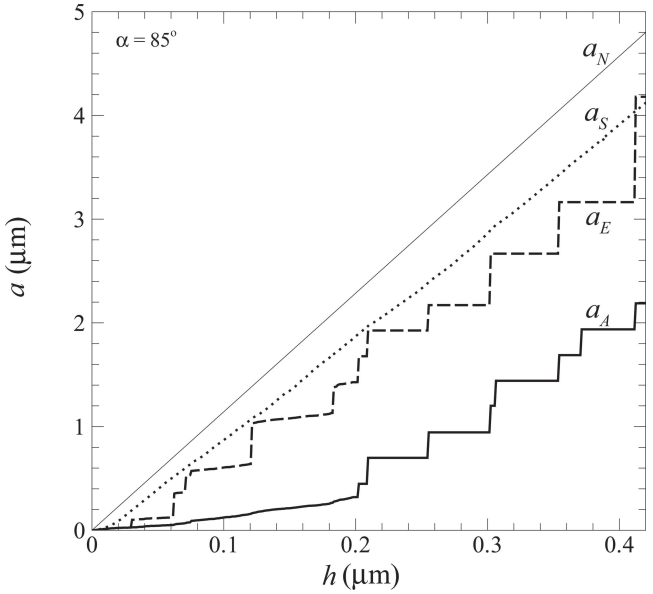

FIG. 7. Evolution of the four contact length measures (a_N, the nominal contact area; a_S, the Oliver–Pharr estimate; a_E, the end-to-end contact area; and a_A the actual contact area) versus depth h for wedge indenters with $\alpha = 85°$.

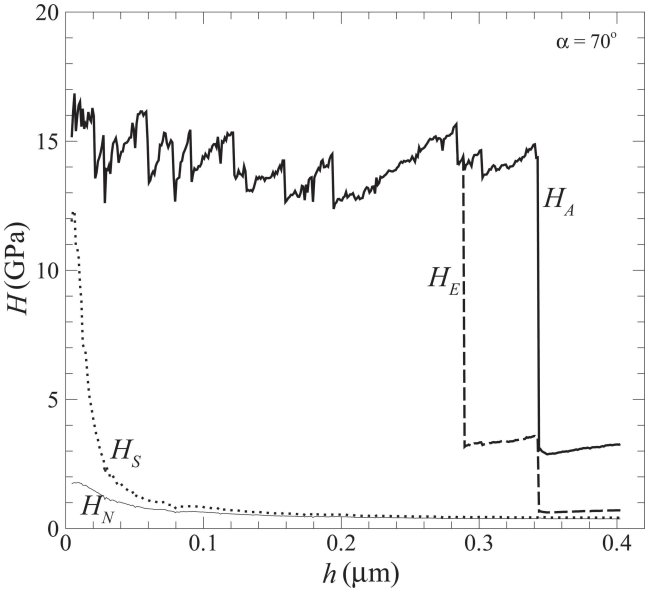

FIG. 8. Hardness versus depth for indenters with $\alpha = 70°$. The various measures with subscripts A, E, S, or N are based on the corresponding contact length measures shown in Fig. 6.

the end-to-end contact length a_E and the actual contact length a_A is due to the evolving surface roughness. In the $\alpha = 70°$ calculation, when the contact length is small, but after plastic flow has occurred, the difference between a_E and a_S is relatively large because the sink-in is dominated by plasticity; the surface remains smooth up to depths of around 0.3 μm where $a_E = a_A$. For the shallower indenter, $\alpha = 85°$, where the contact length is larger, the end-to-end length agrees reasonably well with the contact length a_S over the entire range of indentation depths.[14] However, the true contact length, accounting for roughness, a_A is about 50% smaller.

The hardness H, indentation force per contact length, is given by

$$H = \frac{F}{a} \quad . \tag{14}$$

We denote the hardnesses calculated from contact lengths a_A, a_E, a_S, and a_N by H_A, H_E, H_S, and H_N, respectively.

As seen in Figs. 6 and 7, before the onset of plasticity, the values of a_A, a_E, and a_S are identical or very close, but significantly less than a_N because of elastic sink-in. As a consequence, in the elastic range H_N is smaller than H_S, and $H_A = H_E$. After plasticity has started, the hardness versus indentation depth curves based on the various contact length measures are rather different, with the hardness values H_A and H_E being greater than H_S and H_N. This is seen in particular in Fig. 8 for $\alpha = 70°$. However, as indentation proceeds and more jumps in contact length occur (Fig. 7), the values of H_A and H_E decrease and become closer to the values of H_S and H_N, in particular for $\alpha = 85°$ (Fig. 9). For this shallow indenter, the indentation size effect is significant, while for the $\alpha = 70°$ indenter, neither H_A and H_E exhibit a size effect for indentation depths less than about 0.25 μm.

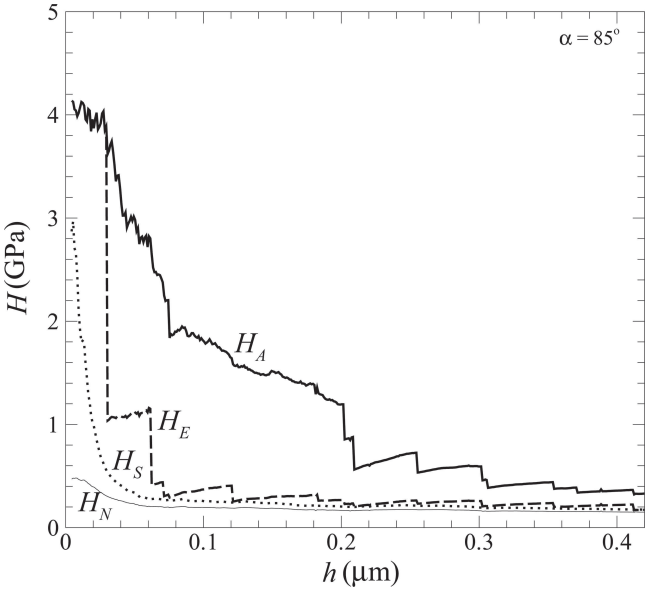

FIG. 9. Various hardness measures versus depth for $\alpha = 85°$.

VII. SURFACE ROUGHNESS

The discreteness of dislocation plasticity produces jumps in displacement at the surface. Individual dislocations exiting a crystal induce displacement jumps of a

magnitude equal to the length of the Burgers vector. However, the motion of many dislocations often gives rise to one or more shear bands. When a shear band extends to the surface, it causes a significant step in the surface profile, leading to significant roughness.

Although in the calculations here, the initial surface is flat, surface roughening causes jumps in contact length, which is what gives the difference between the actual contact length a_A and the end-to-end length a_E, as schematically shown in Fig. 3. To illustrate this further, the profile of the indented surfaces is shown in the insets of Figs. 10 and 11. Here, the jumps in contact length in Figs. 6 and 7 are due to the roughness of the indented surface, and the large steps at the surface are caused by shear bands. The contact with the $\alpha = 85°$ indenter is seen to be relatively smoother since there is a lower density of shear bands, consistent with the relatively small difference between a_A and a_E compared to that for the indenter with $\alpha = 70°$ (compare Figs. 7 and 6).

The slip distributions plotted in Figs. 10 and 11 are computed from

$$\Gamma = \sum_{\beta=1}^{3} |\gamma^{(\beta)}| \quad , \tag{15}$$

where $\gamma^{(\beta)}$ is given by

$$\gamma^{(\beta)} = s_i^{(\beta)} \epsilon_{ij} m_j^{(\beta)} \quad . \tag{16}$$

Here $s_i^{(\beta)}$ and $m_j^{(\beta)}$ are the slip system tangential and normal unit vector of slip system β, respectively. The strains ϵ_{ij} are computed as

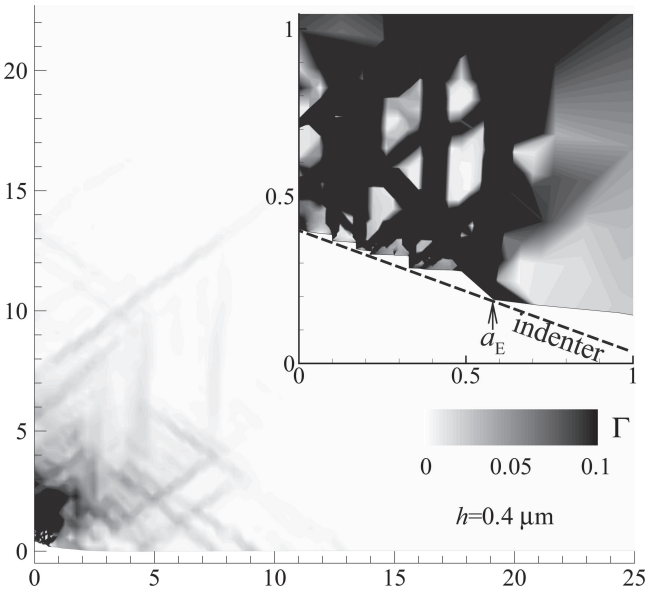

FIG. 10. Total slip Γ distribution and surface profile under a wedge with $\alpha = 70°$ at $h = 0.4$ μm. Distances are in micrometers. The inset shows a zoom of the near-contact region, with the current value of a_E indicated.

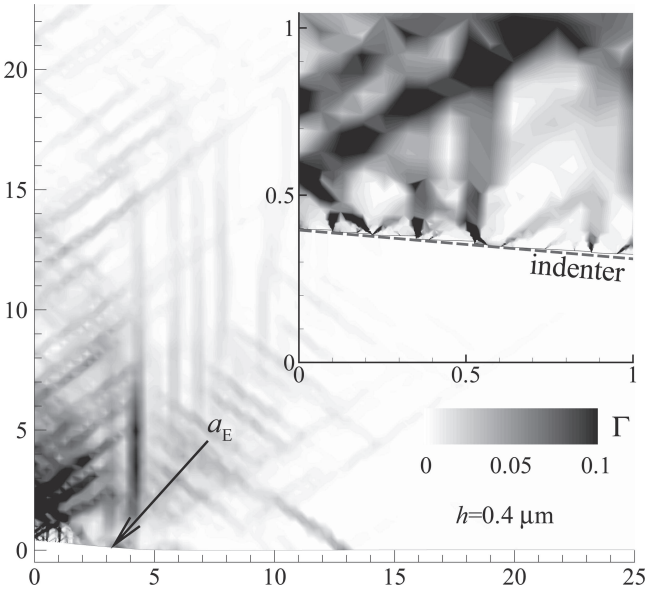

FIG. 11. Total slip Γ distribution and surface profile of wedge $\alpha = 85°$ discrete dislocation indentation calculation at depth $h = 0.4$ μm. Distances are in micrometers. The inset shows a zoom of the near-contact region, with the current value of a_E indicated.

$$\epsilon_{ij} = \frac{1}{2}\left(\frac{\partial u_i}{\partial x_j} + \frac{\partial u_j}{\partial x_i}\right) \quad , \tag{17}$$

from the finite element interpolated displacements u_i. This procedure smears out the intrinsic dislocation discontinuities over single elements, but since the elements near the contact region are as small $2b$, the resolution is still quite high. Figures 10 and 11 show that the plastic zone for $\alpha = 85°$ is substantially larger than that for $\alpha = 70°$ at the same indentation depth.

VIII. DISCUSSION

The value obtained for the indentation hardness is very sensitive to the definition of contact length. In the discrete dislocation computations here, the Oliver–Pharr estimate of contact length a_S obtained from the unloading stiffness using the Oliver–Pharr procedure overestimates the contact length in the small indentation depth regime and thus underestimates the hardness H_S and the indentation size effect. The difference between a_E and a_S arises from the assumption that sink-in of the surface is caused by elastic deformation, while in the discrete dislocation calculations sink-in of the surface is not only caused by elastic deformation but also by plasticity.[14] This is most clearly seen for the indenter with $\alpha = 70°$, which is a tip angle that is similar to that of a Berkovich indenter used experimentally. In fact, for this tip angle, H_E and H_A do not exhibit an indentation size effect until depths of around 0.3 μm, whereas on the basis of the Oliver–Pharr measure H_S, one would infer that there is a size effect in this regime.

The analyses here are 2D plane strain analyses, and there are several important differences between 2D and 3D indentation. First, we expect that the roughening in our 2D calculations is an overestimate since: (i) the Burgers vector always lies in the same (x_1–x_2) plane as the normal to the indenter, and (ii) the displacement jump extends across the entire width (normal to the x_1–x_2 plane) of the indenter side. With more slip systems available in 3D and dislocations beneath the indenter being curved,[10] it is expected that the normal component of displacement jump per unit area of indenter surface will be smaller. Hence, it is likely that actual contact area in 3D indentation and the outer envelop of all contact patches (the equivalent of the end-to-end contact length) may not be as different as the actual and the end-to-end contact length are in 2D. Another potentially important issue is that the scaling with contact stiffness is significantly different between 2D and 3D. While S scales with $E\sqrt{h}$ for self-similar indenters in 3D,[15] the contact stiffness in 2D is independent of h (apart from non-self-similar effects). This suggests the possibility that the Oliver–Pharr estimation technique may be more accurate in 3D than it is in 2D.

IX. CONCLUSION

We have performed plane strain indentation calculations of a single crystal with three slip systems, using rigid indenters with wedge half-angles of $\alpha = 70°$ and 85°. Small strain calculations were carried out, but the contact length is determined in the deformed surface of the material. The crystal has a distribution of sources and obstacles on the slip planes but is initially dislocation free. The predicted hardness decreases with increasing indentation depth, and this size effect is stronger for $\alpha = 85°$ than for $\alpha = 70°$.

The shear bands that extend to the material surface cause the development of surface roughness as indentation progresses. The surface roughness yields jumps in contact, and therefore to a difference between actual contact length a_A and end-to-end contact length a_E. The estimated contact length a_S based on the Oliver–Pharr[15] technique differs from the end-to-end contact length a_E due to the assumption that the sink-in is due only to elastic deformation, which is not the case in the discrete dislocation calculations.

The value of the computed hardness is strongly dependent on the contact area definition. In general, the hardness based on the nominal contact area is smallest while actual rough contact area leads to the highest hardness. The variations in the estimated hardness depending on the definitions of the contact area are substantial at small depths, but the difference diminishes with increasing indentation depth. For the shallow indenters with $\alpha = 85°$, all definitions lead to the usual size effect, but for $\alpha = 70°$, the usual size effect is not observed up to indentation displacements of many hundred nanometers when the hardness is based on the actual contact length.

ACKNOWLEDGMENTS

This research is supported financially by the Netherlands Organization for Scientific Research (NWO) under Project No. 635.000.007. A. Needleman is pleased to acknowledge support from the Materials Research Science and Engineering Centers (MR-SEC) Program of the National Science Foundation under award DMR-0520651.

REFERENCES

1. Q. Ma and D.R. Clarke: Size dependent hardness of silver single crystals. *J. Mater. Res.* **10,** 853 (1995).
2. J.G. Swadener, E.P. George, and G.M. Pharr: The correlation of the indentation size effect measured with indenters of various shapes. *J. Mech. Phys. Solids* **50,** 681 (2002).
3. Y. Wei and J.W. Hutchinson: Hardness trends in micron scale indentation. *J. Mech. Phys. Solids* **51,** 2037 (2003).
4. J. Lou, P. Shrotriya, T. Buchheit, D. Yang, and W.O. Soboyejo: Nanoindentation study of plasticity length scale effects in LIGA Ni microelectromechanical systems structures. *J. Mater. Res.* **18,** 719 (2003).
5. T. Zhu, J. Li, K.J. Van Vliet, S. Yip, and S. Suresh: Simulation of nanoindentation via interatomic potential finite element method. *Comp. Fluid Solid Mech.* **1–2,** 795 (2003).
6. W.D. Nix and H. Gao: Indentation size effects in crystalline materials: A law for strain gradient plasticity. *J. Mech. Phys. Solids* **43,** 411 (1998).
7. M.R. Begley and J.W. Hutchinson: The mechanics of size-dependent indentation. *J. Mech. Phys. Solids* **46,** 2049 (1998).
8. R.K. Abu Al-Rub and G.Z. Voyiadjis: Analytical and experimental determination of the material intrinsic length scale of strain gradient plasticity theory from micro- and nano-indentation experiments. *Int. J. Plast.* **20,** 1139 (2004).
9. S. Qu, Y. Huang, G.M. Pharr, and K.C. Hwang: The indentation size effect in the spherical indentation of iridium: A study via the conventional theory of mechanism-based strain gradient plasticity. *Int. J. Plast.* **22,** 1265 (2006).
10. M.C. Fivel, C.F. Robertson, G.R. Canova, and L. Boulanger: Three-dimensional modeling of indent-induced plastic zone at a mesoscale. *Acta Mater.* **46,** 6183 (1998).
11. H.G.M. Kreuzer and R. Pippan: Discrete dislocation simulation of nanoindentation. *Comp. Mech.* **33,** 292 (2004).
12. H.G.M. Kreuzer and R. Pippan: Discrete dislocation simulation of nanoindentation: The effect of statistically distributed dislocations. *Mater. Sci. Eng., A* **400–401,** 460 (2005).
13. A. Widjaja, E. Van der Giessen, and A. Needleman: Discrete dislocation modelling of submicron indentation. *Mater. Sci. Eng., A* **400–401,** 456 (2005).
14. D.S. Balint, V.S. Deshpande, A. Needleman, and E. Van der Giessen: Discrete dislocation plasticity analysis of the wedge indentation of films. *J. Mech. Phys. Solids* (2006, in press).
15. W.C. Oliver and G.M. Pharr: An improved technique for determining hardness and elastic-modulus using load and displacement sensing indentation experiments. *J. Mater. Res.* **7,** 1564 (1992).
16. W.C. Oliver and G.M. Pharr: Measurement of hardness and elastic

modulus by instrumented indentation: Advances in understanding and refinements to methodology. *J. Mater. Res.* **19,** 3 (2004).
17. E. Van der Giessen and A. Needleman: Discrete dislocation plasticity, *Handbook of Materials Modeling. Volume I: Methods and Models*, edited by S. Yip (Springer, Dordrecht, The Netherlands, 2005), pp.1115–1131.
18. E. Van der Giessen and A. Needleman: Discrete dislocation plasticity: A simple planar model. *Model. Simul. Mater. Sci. Eng.* **3,** 689 (1995).

APPENDIX

The shape factor η in the Oliver–Pharr relation (6) for contact stiffness is determined for wedge indenters from a purely elastic indentation calculation for the block in Fig. 1 having the same dimensions and boundary conditions as those used in the discrete dislocation plasticity analyses. At any h, the elastic sink-in depth h_S is computed from the predicted end-to-end contact length a_E as

$$h_S = h - a_E \cot \alpha \quad .$$

With F and the corresponding $S = dF/dh$ obtained from Eq. (8), the value of η is calculated from Eq. (6) as

$$\eta = \frac{Sh_S}{F} \quad .$$

The resulting $\eta(h)$, shown in Fig. A1, is essentially the same for $\alpha = 70°$ and $\alpha = 85°$. The sawtooth-like behavior of η is caused by the discrete steps in a_E due to the finite element mesh. Smoothing of $\eta(h)$ is done by fitting the function

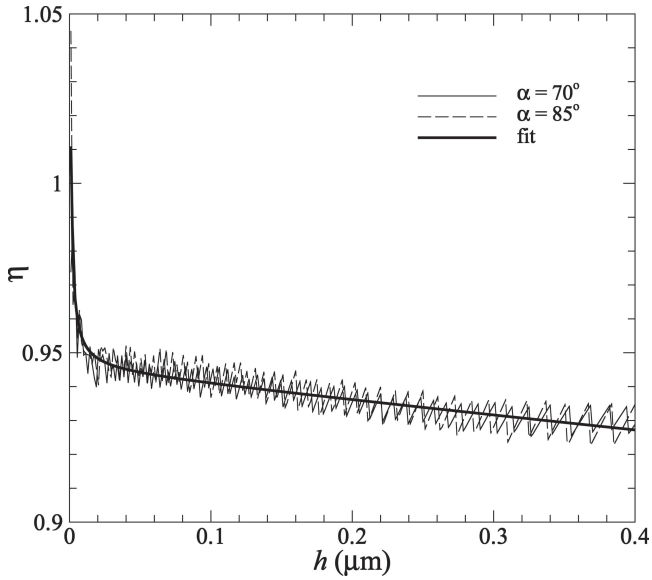

FIG A1. Shape factor η versus depth h of elastic wedge indentation and its fit.

$$\eta(h) = \frac{D_1 + D_2 h}{1 + D_3 h + D_4 h^2} \quad ,$$

to the average value of η of $\alpha = 70°$ and $\alpha = 85°$. The fitting parameters D_1 through D_4, with correlation coefficient $r^2 = 0.891$, are given in Table I, and the fit is shown in Fig. A1.